Composite structure failure analysis post Lithium-Ion battery fire

Sterling, J., Tattersall, L., Bamber, N., De Cola, F., Murphy, A., & Millen, S. L. J. (2024). Composite structure failure analysis post Lithium-Ion battery fire. *Engineering Failure Analysis*, *160*, Article 108163. https://doi.org/10.1016/j.engfailanal.2024.108163

Published in:
Engineering Failure Analysis

Document Version:
Publisher's PDF, also known as Version of record

Engineering Failure Analysis 160 (2024) 108163

Contents lists available at ScienceDirect

Engineering Failure Analysis

journal homepage: www.elsevier.com/locate/engfailanal

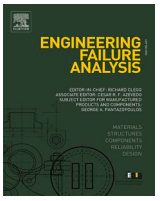

Composite structure failure analysis post Lithium-Ion battery fire

J. Sterling [a], L. Tattersall [b], N. Bamber [b], F. De Cola [b], A. Murphy [a], S.L.J. Millen [a,*]

[a] School of Mechanical and Aerospace Engineering, Queen's University Belfast, Ashby, Building, Belfast, Northern Ireland, U.K. BT9 5AH
[b] WAE Technologies Limited, Grove, Wantage, Oxfordshire, OX12 0DQ

ARTICLE INFO

Keywords:
Mechanical Engineering
Carbon Fibre-Reinforced Polymer (CFRP)
Composites
Finite Element Analysis
Delamination
Lithium-ion Battery Thermal Runaway
Battery Enclosure

ABSTRACT

The use of composite materials has expanded significantly in a variety of sectors. In road transport, lithium-ion batteries (LIB) are the most commonly used. It is standard practice for batteries to be housed within a metal enclosure, which protects and enables extinguishment in the event of Thermal Runaway (TR). Composite materials have been shown to contribute to lightweighting in many vehicle structures and their use in battery enclosures has been growing in recent years - with the aim of reducing the weight of the battery assembly and positively impacting vehicle range. This work develops Finite Element (FE) models to assess thermal and mechanical damage and failure mechanisms during a TR event considering a section of a composite battery enclosure. Experimental data for a cylindrical 18650 lithium-ion battery fire is studied and used to define representative thermal loading. This validated loading profile is applied to a composite specimen and material temperature data is used to appraise damage. Finally, the predicted damage is used to predict and quantify the residual failure mechanism and strength of the specimen post battery fire. Results have shown the presence of damage from a single cell runaway can potentially reduce the strength of the specimen by 20% while multi-cell runaway can potentially reduce the strength by 56%. The predictive simulation capability herein could be used as a design tool for battery fire protection of composite enclosures, potentially reducing the need for corrective action, minimising the number of physical tests to support design and certification, as well as aiding in the interpretation of physical test results.

1. Introduction

The use of composite materials has expanded significantly in a variety of industries including aerospace and electric vehicles (EVs). Battery Electric Vehicles (BEVs) are becoming ever more popular and by far the most popular battery type used in BEVs is the lithium-ion battery (LIB) [1,2]. Every energy source has dangers associated with it and the most relevant for LIBs is thermal runaway, the phenomenon when a battery enters a state of uncontrolled, self-heating, producing very high temperatures, smoke, and even battery fire (plasma) [3–6].

Thermal runaway can occur for several reasons, from an internal short circuit, to mechanical abuse, to rapid charging or over charging of the cell [7,8]. The different phases of thermal runaway have been established through experimentation, for example Fu et al. [9] exposed an 18650 lithium-ion battery to various degrees of incident heat flux and monitored its response. The thermal runaway process has been summarised into a number of distinct stages [9,10]:

* Corresponding author.
E-mail address: scott.millen@qub.ac.uk (S.L.J. Millen).

https://doi.org/10.1016/j.engfailanal.2024.108163
Received 15 December 2023; Received in revised form 7 February 2024; Accepted 23 February 2024
Available online 24 February 2024

- Stage 1: The plastic packaging surrounding the LIB begins to melt and gases are generated within the battery cell, causing swelling, due to an incident heat flux which gradually increases the surface temperature of the cell. The gas release vent cracks and a small amount of gas is released,
- Stage 2: Simultaneously, the solid electrolyte interface (SEI) layer (the layer through which lithium ions move from the cathode to the anode) decomposes exothermically and releases further heat. The electrolyte is able to pass through the broken SEI film and reach the lithiated electrode, forming a new secondary SEI layer. Due to rising temperatures, this new layer ultimately decomposes too, releasing additional heat,
- Stage 3: A violent reaction occurs between the lithium released from the decomposition of the electrodes, and the by-products of the electrolyte decomposition, which generates huge quantities of heat energy within a short amount of time. This results in an explosion, ejecting the cap assembly and large amounts of gas, which are subsequently ignited. This event can be seen as a sharp rise in surface temperature from 250 °C to 750 °C within ~ 10s,
- Stage 4: Following the explosion, the temperature gradually declines as the chemical fuels are exhausted by the fire.

Arcing discharge during thermal runaway or otherwise is also possible in lithium-ion batteries [11,12]. However, this particular phenomenon is not well studied in the open literature.

Fig. 1a shows a sectional diagram of an 18650 cell from ref. [13] while Fig. 1b shows the generalised temperature profile for an 18650 cell undergoing thermal runaway, adapted from ref. [9], with the different stages of thermal runaway marked on the plot. A number of works have attempted to model the thermal runaway process [14,15]. For example, Lamb et al. [15] examined the behaviour of small modules after thermal runaway was induced in a single cell. The authors were able to determine the order in which cells underwent thermal runaway.

As noted earlier, it is necessary to enclose batteries, to shield people, systems, and structures from their stored energy and to also protect the batteries. Thus, it is standard practice for the batteries on a BEV to be housed within an enclosure which is typically made from aluminium or steel [16]. However, both aluminium and steel add weight to the battery assembly, adversely affecting the range of the EV. It is important to minimise the weight of the battery enclosure where possible, whilst not compromising on safety [17]. As a result, due to their ability to contribute to lightweighting, the use of composites in the construction of battery enclosures has been growing in recent years, in both commercial automotive and motorsport sectors [18,19]. Research has been completed to assess the impact resistance of composite structures containing lithium-ion batteries [19–23] while other works have applied compressive, tensile, or three-point loading to multifunctional composite structures with embedded batteries [24].

1.1. Composites exposed to fire

There is a significant body of research on the exposure of composites to fire [25–29]. When a composite is exposed to fire, or any rapid heating, damage is produced which can include fibre fracture, matrix cracking, delamination, char formation and fibre blow-out [30]. Some works have sought to establish the fire reaction properties (time-to-ignition, flame spread, and heat release rate characteristics) [26] while others focus on the structural fire behaviour or performance of composites during or post fire (stiffness and strength) [27,29,31]. The effect of fire on composites has been studied using both experimental and simulation approaches. Experiments have typically been conducted on representative structures [31,32] but while these tests can determine the mechanical integrity and burn through resistance, they are expensive, complicated, and cannot be easily extrapolated to other fire scenarios [25].

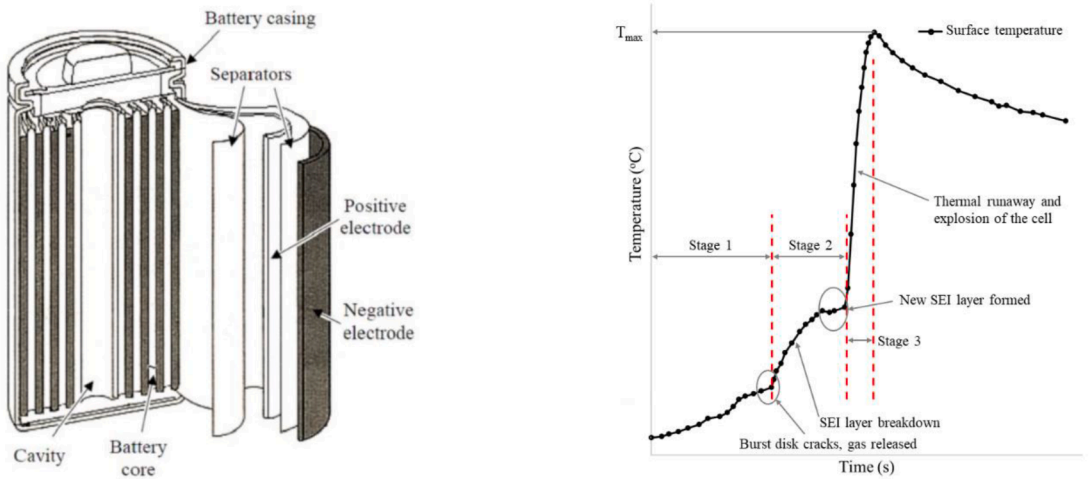

a) Sectional diagram of an 18650 cell *b) Generalised temperature profile for 18650 cell*

Fig. 1. Diagrams showing a) sectional diagram of an 18,650 cell from ref. [13] and b) generalised temperature profile for an 18,650 cell undergoing thermal runaway, adapted from ref. [9].

In literature, models have been presented which analyse the thermal, chemical, physical, and failure processes that control the structural responses of mono-laminates and sandwich composite materials in fire [25]. The majority of thermal models in literature have applied one-sided heating by fire to the specimen and determined the resulting temperature distribution through the composite [29,31,33]. Much research work has been undertaken to investigate composite fire behaviour under compressive loading [27,34], mainly due to structural application, while other works have focussed on tensile loading [28,29,33]. As noted by Mouritz et al. [25], it is common practice for the fire to be decoupled from the composite i.e. the initiation and growth of the fire is not considered in the analysis. Rather, it is assumed that the composite surface is heated under controlled heat flux or temperature conditions. The advantage of this approach is that it reduces the computational expense since thermal loading and structural decomposition are decoupled. However, the disadvantage is the chemical reactions of the fire are not represented in the model, only the resulting thermal loading is captured.

1.2. Summary

The conventional methodology to test the structural response of composites involves physical experimentation subjecting models to loading representative of real structural applications, such as fuselage sections of aircraft or composite train car bodies subjected to large scale fire tests. However, while these tests provide crucial data on mechanical integrity and burn through resistance, they are expensive, complex, and difficult to extrapolate and apply to other fire scenarios. As a result, the benefits to achieving reliable fire analysis modelling are clear [25].

The use of lithium-ion batteries is increasing in many sectors and understanding the effect of thermal runaway is of growing importance. Therefore, to ensure structural integrity, it is standard practice for EV batteries to be housed within a metal enclosure. However, it is important to minimise the weight of the battery enclosure to positively impact vehicle range, therefore, lightweight alternatives can be investigated. The use of composite materials for lightweight battery enclosures has the potential to positively impact vehicle range. However, the behaviour of composites in fire is less desirable than traditional metallic structures, and the effect of a LIB fire on a composite structure has not been investigated.

The use of heat transfer and thermo-mechanical simulations is common in other areas of published research, e.g. lightning strikes. However, one area of limited research is the effect of runaway and LIB fire on the structural performance of composite battery containment. Research has been completed to assess the impact resistance of composite structures containing batteries and the compressive strength of fire damaged composites. However, little can be found in open literature about the combined effect of mechanical and thermal loading, specifically caused by a LIB thermal runaway event.

This paper provides a simulation framework, validated against single cell tests, that can be used to predict the damage to composite

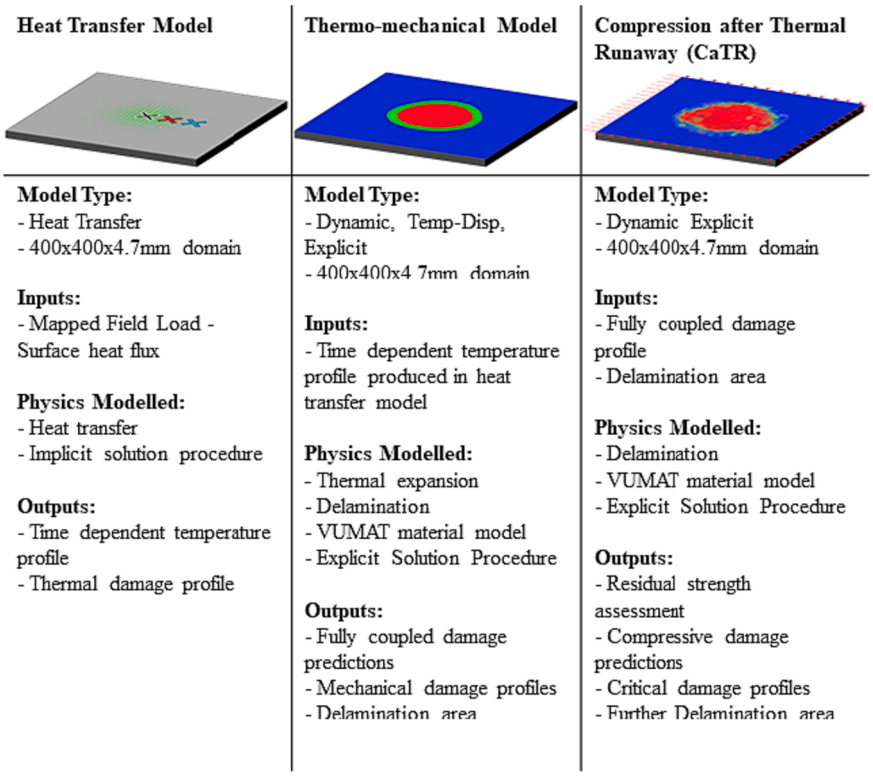

Fig. 2. Model flow scheme with corresponding inputs and outputs for composite specimen.

materials generated during a LIB thermal runaway. Therefore, this paper will complete a number of sequential simulations to predict the potential thermal and mechanical damage from a LIB runaway event before predicting the resulting residual strength reduction for a composite containment panel. The battery cell considered in this work is a cylindrical 18650 type. Firstly, a thermal loading approach will be created and validated against experimental data before this is applied to a composite specimen. Sequential heat transfer and thermo-mechanical models will then be used to predict damage, before Compression after Thermal Runaway (CaTR) simulations will predict the failure mechanism and residual strength of the specimens.

2. Methodology

In order to predict the CaTR failure mechanism and residual strength of composite specimens, an appropriate set of simulations was assembled based on existing open literature. Fig. 2 shows an analysis workflow assembled for the work herein. This workflow of simulations provides a computationally efficient package for the numerical study of thermal runaway tolerance in laminated composites. When combined with a single set of material data and battery thermal runaway loading definitions, this approach allows for the study of thermal and mechanical damage and residual compressive strength.

In Fig. 2, the first step in the sequential analysis procedure is modelling of the heat transfer behaviour due to heat flux loading. The results from heat transfer simulations are transferred to structural models to predict mechanical damage (i.e., fibre/matrix failure or delamination), considering strain and heating rates. Finally, the CaTR strength is predicted using Abaqus/Explicit with a VUMAT subroutine after damage mapping with python scripts. Each model will now be discussed in more detail.

2.1. Initial loading development and validation

In order to study the fire resistance of battery enclosures it was necessary to develop a Finite Element Model (FEM) which can capture the spatial and temporal variation of a battery fire. Therefore, a model was developed to replicate the experimental work of Zhang et al. [35]. A transient heat transfer simulation was developed in Abaqus/Standard with a 6061 aluminium alloy plate measuring 400 mm x 400 mm x 3 mm. DC3D8 8-node linear brick solid heat transfer elements were used within heat transfer simulations. Since the purpose of this heat transfer model was to predict only the temperature distribution in the specimen, boundary conditions such as simple supports or elastic material properties were not included in this analysis type, as they would not affect the predicted temperature distribution.

The governing equation for heat conduction in this simulation is expressed as:

$$\rho C_p \frac{\partial T}{\partial t} = \nabla.(k\nabla T) = \frac{\partial}{\partial x}\left(k_x \frac{\partial T}{\partial x}\right) + \frac{\partial}{\partial y}\left(k_y \frac{\partial T}{\partial y}\right) + \frac{\partial}{\partial z}\left(k_z \frac{\partial T}{\partial z}\right) + q_v \quad (1)$$

where T is temperature (^{o}C), t is time (s), k is thermal conductivity of the material (W/mK), ρ is density (kg/m^3), q_v is the rate of energy generated per unit volume (W/m^3) and C_p is the specific heat capacity (J/kgK).

While this specimen arrangement represents a similar testing scenario to the UL2596 test standard [36], the A36 structural steel box will not be modelled in this study. Only a single side of a box is modelled to represent the experimental arrangement in ref. [35]. Isotropic temperature dependant material properties for 6061 aluminium alloy are shown in Table 1, from refs. [37,38].

A predefined field was used to assign an ambient temperature of 25 °C at the start of the simulation and a temperature dependant surface film condition was applied to the rear, unheated face of the plate while thermal radiation was included on the front face with an emissivity of 0.15 [39].

Data on the heat flux magnitude over time for an 18650-cell undergoing TR is scarce and as such the experimental results from Shen [40] were chosen as an appropriate source. This plot conveys the heat flux behaviour of a battery during Stage 3 of TR, the most violent and largest release of energy. However, as the plot only provides information up to 6 s after the initial explosion, it was necessary to extrapolate the heat flux beyond this point in order to obtain a match between the temperature profiles on the rear plate in the FE model and those measured by Zhang et al. [35] using thermocouples.

In addition to varying over time, the magnitude of the heat flux varies spatially. At the time of writing little work has been done on calculating the heat flux released from LIBs at different spatial locations, therefore experimental information from the work of Zhang et al. [35] can be used to derive the spatial variation.

Zhang et al. [35] calculated the total heat flux from flame-to-plate due to convection and radiation at three distinct positions on the

Table 1
Temperature dependant material properties of 6061-T6 aluminium alloy.

Temperature (°C)	Specific Heat (J/kgK)	Thermal Conductivity (W/mK)	Density (kg/m^3)
25	917	162	2690
93	978	177	2690
201	1028	192	2660
316	1078	207	2630
428	1133	223	2602
571	1230	253	2574

plate (X = 0, 50, and 100 mm) and at different plate heights. As this study considers the worst-case scenario, heat flux data at a plate height of 20 mm was chosen as most suitable. The positions of X = 0, 50, and 100 mm are marked by black, red, and blue crosses, respectively on Fig. 3b and correspond to the thermocouples T8, T9 and T10, respectively in the corresponding experiments in ref. [35].

The heat flux distribution was applied to the model using a mapped analytical field in Abaqus. This allowed the precise heat flux magnitude to be specified at discrete locations across the surface of the plate. The load options of mapped field and amplitude are highlighted in red in Fig. 3a and the resultant representation is shown by the loading arrows on the model, Fig. 3b and Fig. 3c. This was a non-trivial exercise and required numerous iterations of both the loading profile and the FE mesh to achieve the correct temperature distribution on the rear plate surface which matched that reported in the experimental paper.

A mesh convergence study was carried out on the aluminium plate assessing the effects of changes to the mesh on the three thermocouples T8, T9 and T10. The maximum difference in the predicted and experimental temperature at these thermocouples was used as the convergence criteria. The number of elements through the thickness had a negligible effect on predictions but the global seed size was more important. Therefore, the resulting mesh used for this study had a global seed size of 10 mm and three through thickness elements since this had the smallest errors and most accurate predictions at T8, at the centre of the specimen, where maximum flux and damage would occur.

Fig. 4 compares the back face temperatures at 0 mm, 50 mm and 100 mm from the centre of the plate, measured experimentally by Zhang et al. [35] (indicated by "_Exp") and the predictions using the loading approach and converged mesh established herein (indicated by "_Sim").

The criteria for acceptable thermocouple predictions was the peak temperature and this was achieved through manual iterative improvements of the mapped field loading profile. It can be seen there is good agreement between the measured and predicted temperature peaks. However, there is some discrepancy 50 mm from the centre of the plate around 3 s into the simulation. This would suggest the loading magnitude at this point is too large or the inherent velocity of the flame is not captured correctly. This could be improved by further CFD analysis, though this is beyond the scope of the present work. The predictions can still be considered acceptable given that the general trends are captured and the peak temperatures are within 5.5% across the thermocouples. In addition, there was no repeat data in the referenced experimental work and since no two fires will be identical there will be some inherent variation in results from test to test.

Unlike the UL2596 test standard [36] which requires 25 cells, this initial case study focused on a single cell TR event to match the experiments from Zhang et al. [35]. Once the loading method and input heat flux had been established and validated for a single cell runaway event, the loading was developed to capture the effects of multi-cell runaway.

2.2. Multi-cell thermal loading

In this case, the work of Lamb et al. [15] was used to determine the order of thermal runaway in a module containing ten cells. The

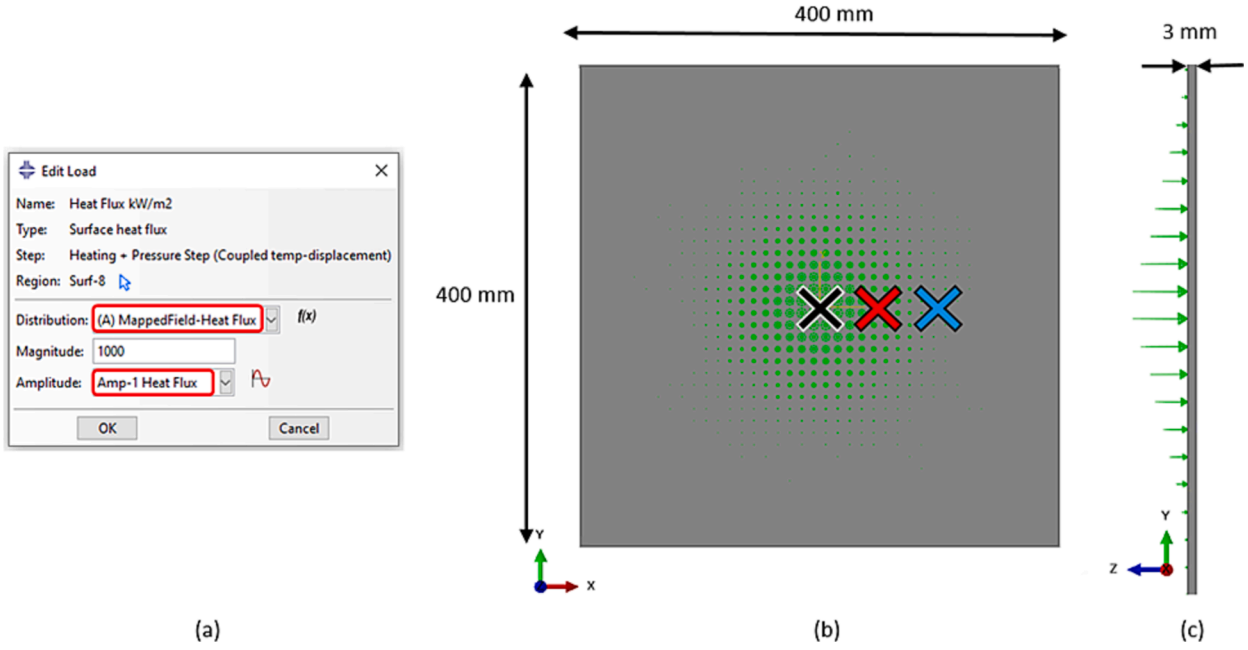

Fig. 3. (a) Application of the custom 'Mapped Field' and 'Amplitude' to the Heat Flux load. (b) Front view of plate with green heat flux load arrows displayed in centre and locations of X = 0, 50, and 100 mm highlighted. (c) Close-up side view of plate displaying green heat flux load arrow distribution. (For interpretation of the references to colour in this figure legend, the reader is referred to the web version of this article.)

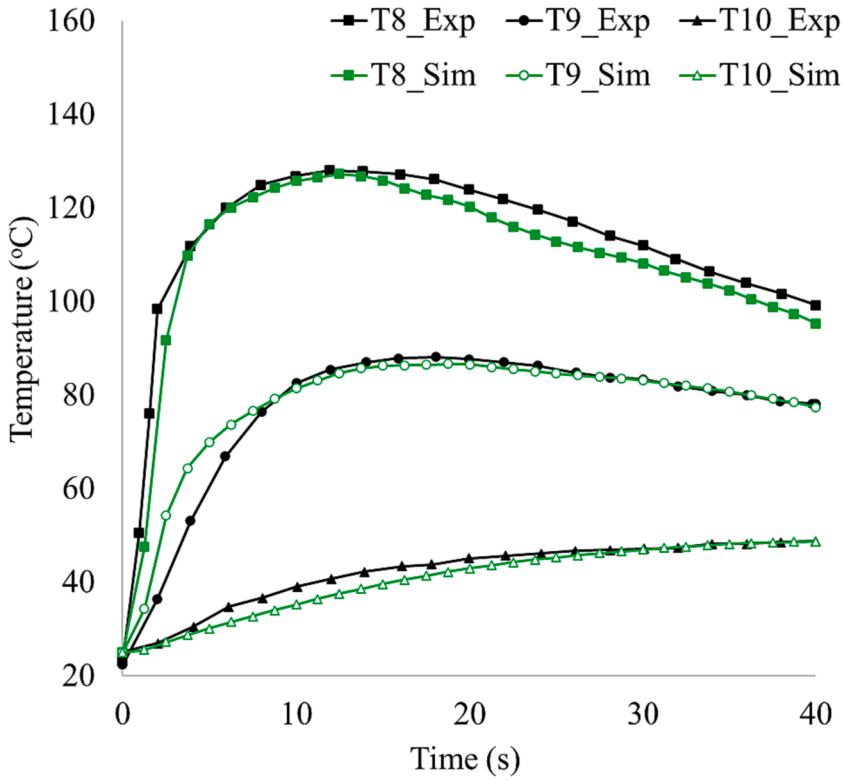

Fig. 4. Comparison of measured (from ref. [35]) and predicted back face temperature on aluminium plate.

cells were positioned in a triangular shape as shown in Fig. 5a. These cells were grouped based on the order of runaway observed in the experiments [15]. Therefore, cell "1" enters runaway first. Twenty seconds later, cells marked "2" enter runaway and a further 20 s later, cells marked "3" enter thermal runaway. A spreadsheet tool was used to map the heat flux loading profile based on the position of each of the ten cells in Fig. 5a. Individual cell coordinate positions are entered and a table of the appropriate mapped field data is automatically calculated, ready for use in the FE model. Fig. 5b shows the top view of the distribution of heat flux across the surface of the specimen for cell 2*.

Multi-cell thermal loading was applied to an aluminium plate and results of this analysis can be found in the Supplementary Material. Subsequent mechanical loading on aluminium specimens was not completed as the focus of this work is the structural response of composite specimens to battery thermal runaway.

Once both single cell and multi-cell battery fire loading profiles had been established, a composite material model was used to determine the effect of LIB fires on the structural response of the composite specimen.

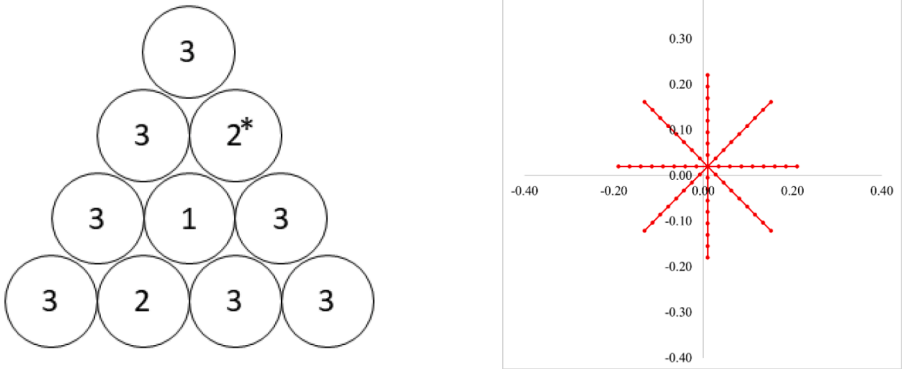

a) Cell runaway order adapted from ref. [15]

b) Calculated mapped field for cell 2*

Fig. 5. (a) Cell positions and runaway order adapted from Lamb et al. [15] and (b) calculated mapped field for cell 2*.

2.3. Study of the fire resistance of CFRP structures

The validated loading profile was applied to a Carbon Fibre Reinforced Polymer (CFRP) structure to assess the failure mechanisms and effect of thermal runaway on damage. The composite specimen was assumed to be an aerospace grade material, IM7/8552. The specimen measured 400 mm x 400 mm, to match the aluminium plate and had a stacking sequence of $[45/0/-45/90]_{4s}$ (where numbers represent the orientation angle, 45 represents the top ply orientation of 45°, subscript numbers outside brackets represent the number of repeats and subscript *s* represents a symmetric laminate). The thickness of each ply was 0.147 mm giving a total specimen thickness of 4.704 mm. Temperature dependant material properties for CFRP are shown in Table 2, from ref. [41].

Damage in composite specimens during thermal simulations is characterised as moderate or severe [30,41]. Moderate damage represents the start of resin decomposition and comprises a broad surface region of shiny resin, matrix cracking and delamination. Further severe damage is likely to be deeper with char residue and fibre fracture. The moderate damage region is captured by the 300 °C temperature contour while the severe damage region is captured by the 500 °C temperature contour. These temperatures capture a delay in the change of state of the material resulting from the rate of change of temperature predicted within the TR event, which is significantly higher than the thermogravimetric analysis used in part to generate the base material properties [30,41]. These temperature ranges are used only for the assessment of thermal damage within the model. For example, any region with a temperature range $0\ °C < T \leq 300\ °C$ can be considered pristine while $300\ °C < T \leq 500\ °C$ is considered moderately damaged and therefore this region would be expected to include shiny resin, matrix cracking and delamination in an experiment.

Changes in material behaviour were accounted for by the temperature dependent material properties, shown in Table 2. ABAQUS user-subroutines HETVAL and USDFLD were used to define the thermal behaviour of the material. HETVAL allows the extent of matrix thermal decomposition to be determined at each time increment, accounting for decomposition kinetics and heat generation. Matrix decomposition is assumed to vary linearly between onset (300 °C) and complete decomposition (500 °C). Material properties are then updated using USDFLD.

A further mesh convergence study was completed for the composite specimen. Convergence was assessed considering the size of the moderate damage (300 °C) contour on the top surface of the specimen and the damage depth. The mesh size was governed by two main criteria; the global seed size (mm) and the number of elements through-the-thickness of each ply. The back surface temperatures of plies one, three and five were also compared.

Examining Table 3, the mesh convergence study indicates that varying the global seed size alone had a minimal impact on the moderate damage area (±6%) and varied the damage depth by a single ply. Global seed size alone changed the ply rear surface temperatures by a maximum of ±8 %. Holding the global seed size constant and varying the number of through thickness elements increased the moderate damage area by a maximum of 8%. The damage depth was similar in all models at either five or six plies deep. The ply rear surface temperatures also had a maximum change of 8%. The chosen mesh had a global seed size of 10 mm with two elements through the thickness of each ply.

2.4. Thermo-mechanical modelling

After the completion of the heat transfer step, a thermo-mechanical model, considering fully coupled thermal-stress analysis was completed with a dynamic, temperature-displacement, explicit analysis step in Abaqus/Explicit using C3D8RT elements (8-node trilinear displacement and temperature, reduced integration with default hourglass control) [42]. This step could predict mechanical damage due to the combined effects of mechanical strain (from dynamic loading) and thermal strain (due to temperature transferred from the previous thermal damage simulation).

In order to capture the heating profile in the thermo-mechanical analysis the temperature profile from each node of each element of the FE mesh in the heat transfer simulation was transferred using Python scripts, as discussed in previous works [41,43]. Thus, the temporal variation in temperature is represented throughout the duration of the thermo-mechanical simulation when predicting delamination and other damage modes.

Intralaminar damage was captured using a VUMAT material model developed by Millen et al. [44]. This material model also

Table 2
Temperature dependent CFRP material properties [41].

			Thermal Conductivity		
Temperature (°C)	Density (kg/m^3)	Specific Heat (J/kg°C)	Fibre (W/m.K)	Transverse (W/m.K)	Through-Thickness (W/m.K)
25	1520	1065	8.00	0.67	0.67
500	1520	2100	4.39	0.34	0.34
800	1100	2100	2.61	0.18	0.18
1000	1100	2171	1.74	0.10	0.10
3316	1100	2500	1.74	0.10	0.10
3334	1.11	5875	1.74	0.10	0.10
		Temperature Range (°C)		Energy Released (J)	
Resin Decomposition		500–800		4.8x10^6	
Fibre Ablation		3316–3334		43x10^6	

Table 3
Mesh convergence table.

	Global seed (mm)	Elements TT (-)	Run time (hrs)	Moderate damage area (mm^2)	Moderate damage depth (plies/mm)	Peak rear face temperature Ply 1	Ply 3	Ply 5
Mesh 1	10	1	0.75	4285.0	6 / 0.882	549	418	338
Mesh 2	15	1	0.38	4012.8	5 / 0.735	527	400	322
Mesh 3	5	1	5.75	4228.9	6 / 0.882	564	426	348
Mesh 4	10	2	1.17	4270.2	5 / 0.735	548	417	338
Mesh 5	10	3	1.25	4224.5	6 / 0.882	591	424	342
Mesh 6	10	4	2.42	3945.2	6 / 0.882	548	417	338

considered strain and heating rates. The Hashin failure initiation criteria was used to predict fibre tensile, fibre compressive and transverse tensile failure. In the transverse and through-thickness directions the Puck criteria was used for compressive failure. In all cases, linear damage evolution behaviour was included which indicated damage when the initiation criteria was greater than 0.99. In order to include strain rate effects, the rate was determined and the strain rate regime (quasi-static, intermediate or high-rate) was used to apply a scale factor to E_2, E_3 and the intralaminar strength and fracture toughness properties. Heating rate effects were included by offsetting the temperature at which the moduli and strength of the material began to degrade. Further details of the development of this model and its implementation are given in ref. [44]. Delamination between neighbouring plies was captured using cohesive surfaces with a bi-linear traction-separation law [44]. The onset of interfacial damage was governed by the quadratic stress criterion and fracture energy dissipation during damage propagation was governed by the Benzeggagh and Kenane (B-K) criterion [45]:

$$G^C = G_n^C + \left(G_s^C - G_n^C\right)\left(\frac{G_s + G_t}{G_n G_s + G_t}\right)^{\eta_{BK}^C} \tag{2}$$

where η_{BK}^C is the mixed-mode interaction and G_n^C and G_s^C are the critical fracture energies required to cause failure in the normal and shear directions, respectively.

In this case, loads, boundary conditions and material properties such as elastic properties and thermal expansion were included. While the temperature distribution was prescribed at each increment, using the temporal variation in temperature from the heat transfer model, the thermo-mechanical response was predicted considering constrained thermal expansion. The specimen was fixed around its perimeter using displacement boundary conditions U1=U2=U3=0. These conditions were used to replicate the possible fixture of the panel within a larger structure.

Material properties for the mechanical analyses are shown in Table 4 and Table 5.

2.5. Residual strength modelling

The final simulation step, Compression after Thermal Runaway (CaTR), was completed using Abaqus/Explicit. The models for the study of CaTR residual strength, shown in Fig. 6, maintained the same specimen dimensions used in the corresponding thermal and thermo-mechanical models. Boundary conditions in the CaTR models were derived from the typical compression-after-impact (CAI) arrangement, shown in red arrows and labels on Fig. 6. In this case the side of the specimen opposite the compression load was fixed in all directions while the two sides perpendicular to loading were constrained to replicate anti-buckling guides.

The mesh in the CaTR models had a refined region with an in-plane seed of 3 mm increasing to 6 mm at the extremes of the plate.

Initially, an undamaged specimen was compressed to achieve a benchmark strength to compare the knockdown effect of TR damage. In the single cell and multi-cell models it was necessary to incorporate thermo-mechanical damage into the simulation prior to the compression step. Therefore, the damage state from the thermo-mechanical models was transferred to the CaTR using the same approach proposed in ref. [46]. In this approach, two forms of damage, mechanical damage to the ply (intralaminar) and delamination (interlaminar) were transferred using Python scripts. Mechanical damage was transferred by analysing areas of element deletion or degraded matrix on each ply, produced as a result of thermal and mechanical strains. Nodal coordinates were extracted to describe the region, converted to element sets and transferred to make equivalent element sets within the CaTR model. The elements in this set were

Table 4
Mechanical properties for thermo-mechanical model [44].

Temperature (°C)	E_1 (MPa)	$E_2 = E_3$ (MPa)	$G_{12} = G_{13}$ (MPa)	G_{23} (MPa)	$\nu_{12} = \nu_{13}$	ν_{23}	α11 ($x10^{-8}$)	α22 = α33 ($x10^{-5}$)
25	161,000	11,400	5170	3980	0.32	0.44	1.8	3
200	161,000	9120	4136	3184	0.32	0.44	5.4	5.25
260	161,000	114	41.36	31.84	0.32	0.44	5.4	5.25
600	161,000	5.7	2.068	1.592	0.32	0.44	5.4	5.25
3316	161,000	5.7	2.068	1.592	0.32	0.44	5.4	5.25
>3316	1610	0.57	0.2068	0.1592	0.32	0.44	5.4	5.25

Table 5
Strength, fracture, and interface properties for thermo-mechanical model [44].

Intralaminar strength and fracture toughness								
Xt (MPa)	Xc (MPa)	Yt (MPa)	Yc (MPa)	$S_{12} = S_{13} = S_{23}$ (MPa)	Γ_{11}^{C} (N/mm)	Γ_{11}^{T} (N/mm)	Γ_{22}^{C} (N/mm)	Γ_{22}^{T} (N/mm)
2723	1200	60	200	95.8	24	80	0.28	1.3
Interface properties								
t_n^0(MPa)	$t_s^0 = t_t^0$ (MPa)	G_n^C(kJ/m^2)	$G_s^C = G_t^C$ (kJ/m^2)					
60	90	0.2	1.0					

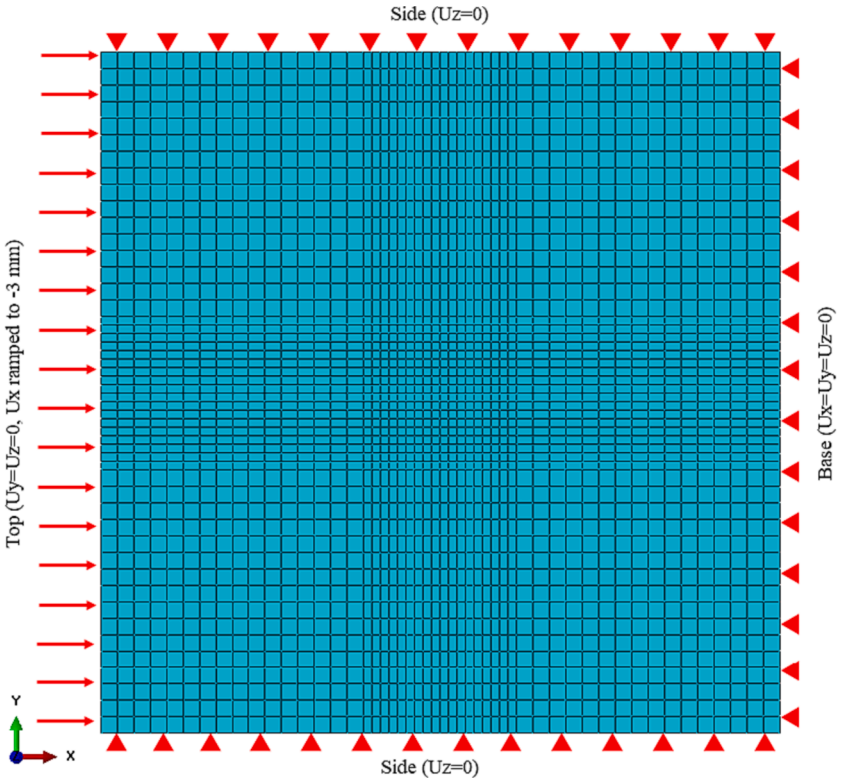

Fig. 6. CaTR simulation mesh and boundary conditions.

then assigned near-zero mechanical properties in the CaTR models. The remaining elements were assigned pristine mechanical properties to represent undamaged regions.

2.6. Assumptions and limitations

The present work focussed on the prediction of damage within a composite structure exposed only to the thermal loading from a cylindrical 18650 type battery thermal runaway event. Battery thermal runaway is a highly dynamic, stochastic, multi-physics problem which can produce significant variation in peak temperatures, heat release rates, and most importantly state of charge of the batteries [47,48]. However, for the sake of model methodology development, this work has assumed a fixed combination of peak temperature, heat release rate, and state of charge from the corresponding experimental works [15,35]. No assessment of the effect of these parameters on damage was conducted in this paper. Rather, this work focused on establishing a modelling framework which could be used in subsequent factorial analysis.

In addition, the models herein account for only thermal loading and presently exclude other multi-physics phenomena, such as pressure loading, generated from the impingement of hot gasses, and electrically charged ejecta, which influence both the surface temperature and flow behaviour of the vented gases. Indeed, the fire behaviour, thermal output, pressure released and the amount and direction of charged ejecta will vary from experiment to experiment producing some inherent variation in results from test to test. Therefore, any multi-physics framework will be truly representative of only a small percentage of battery thermal runaway events. However, such a framework has been demonstrated capable of dealing with other physics [46] and will be modified in future work to

further account for the multi-physics nature of this problem.

3. Results

The discussion of results will first focus on thermal damage and the temperature profile through the relevant specimens. This will be followed by a discussion of the mechanical damage predictions and resulting effect on residual strength.

3.1. Single cell runaway on composite specimen

Initially, heat flux is applied to the top surface of the specimen. The thermal conductivity in the fibre direction is largest and this direction is therefore the optimal conduction path. Some heat conducts in the transverse and through thickness directions due to the difference in conductivity in each direction. As the temperature of each ply increased, matrix thermal decomposition occurred and through-thickness conductivity increased (as the CFRP was converted to a char like state) which allowed heat to reach the second ply and so on. Since less heat flowed into each subsequent ply, the size of the damaged area reduced with each ply through the specimen thickness.

Fig. 7 shows the predicted time dependent front face temperatures at 0 mm, 50 mm and 100 mm from the centre of the plate and the rear face temperature at 0 mm from the centre of the plate for each of the top seven plies during a single cell runaway event. Fig. 7a shows the rapid heating rate of the specimen, approximately 14,000 °C/min. The peak temperature during the simulation was 656 °C, significantly higher than the peak temperature in the aluminium specimen, Fig. 4, 127 °C. As the simulation progresses the peak temperature gradually falls as the incident flux declines and the temperature of the specimen normalises due to thermal conduction and surface emissivity. Fig. 7b also shows the lag in temperature rise in plies through the thickness of the specimen. The red dashed lines on Fig. 7b indicate the start of moderate damage (300 °C) and severe damage (500 °C).

Fig. 8 shows the top surface and cut-view, through-thickness thermal damage profiles after flux loading from the single cell 18650 thermal runaway event. The moderate damage area (areas where 300 °C $\leq$ T $<$ 500 °C) was 10,587 mm^2 and extended four plies deep or 0.588 mm. The severe damage area (areas where T $\geq$ 500 °C) was 5413 mm^2 and was confined to the top ply.

3.2. Multi-cell runaway on composite specimen

Fig. 9 shows the predicted time dependent front face temperatures, at the thermocouple positions only and not experimental data from actual thermocouples, at 0 mm, 50 mm and 100 mm from the centre of the plate and the central, rear face temperature of each of the top twelve plies during a multi-cell runaway event. The red dashed lines on Fig. 9b indicate the start of moderate damage (300 °C) and severe damage (500 °C).

When the first cell enters thermal runaway the temperature at the front face rises rapidly, reaching approximately 1200 °C in around 4.5 s, equivalent to a heating rate of approximately 16,000 °C/min. When the second group of cells enter runaway the front face temperatures see a negligible rise, but temperature is maintained at a steady plateau. However, the observed temperatures through the specimen rise steadily when the second group of cells enter runaway. Once the third group of cells enter runaway, the heat flux impinging on the specimen surface increases dramatically again, heating the specimen at a rate of approximately 24,300 °C/min, and

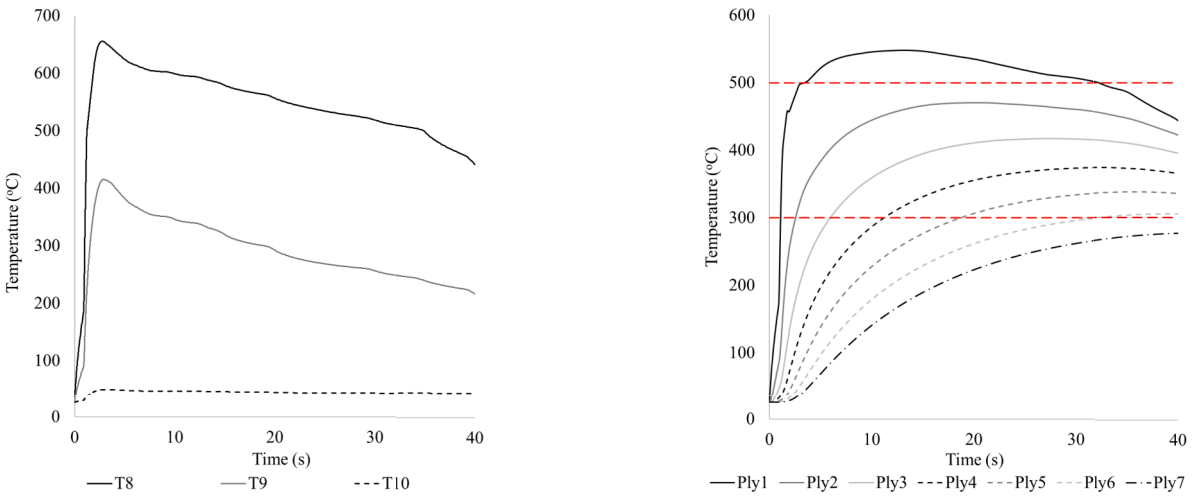

a) Front face thermocouple temperatures

b) Rear face temperatures of each of the first seven plies

Fig. 7. Temperatures recorded at a) thermocouples and b) the rear face (measured at the central nodes) of each of the first seven plies for single cell loading.

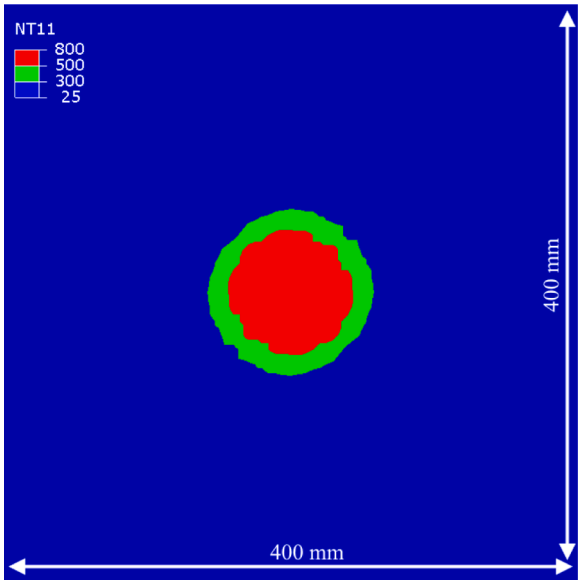

a) Top surface damage profile

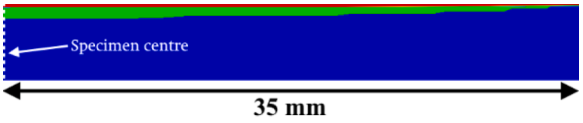

b) Through thickness damage profile

Fig. 8. Top surface and through thickness thermal damage after single cell flux loading (units are ^{o}C).

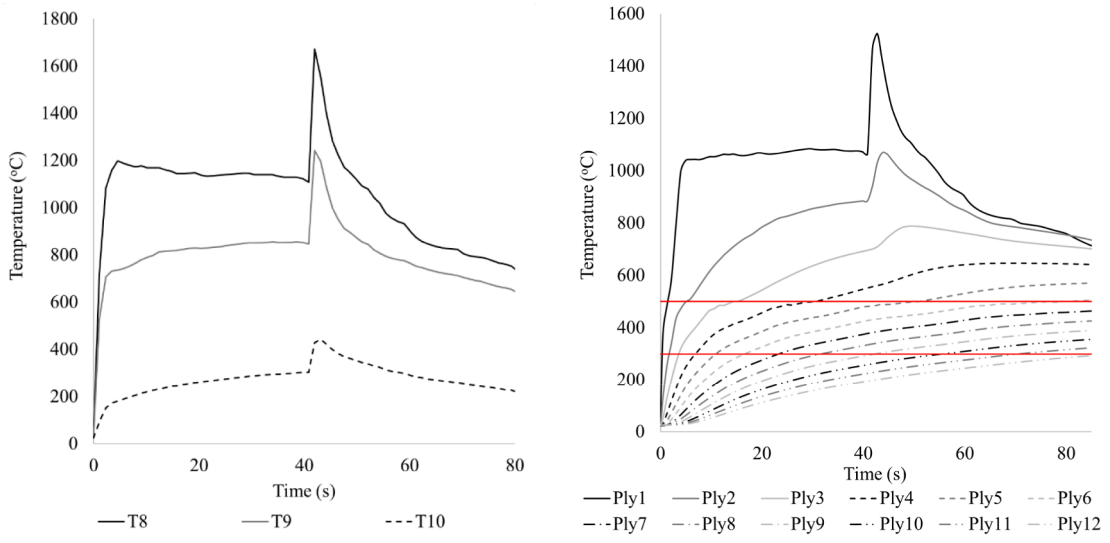

a) Front face thermocouple temperatures

b) Rear face temperatures of each of the first twelve plies

Fig. 9. Temperatures recorded at a) thermocouples and b) the rear face (measured at the central nodes) of each of the first twelve plies for multi-cell loading.

the resulting measured thermocouple temperatures increase significantly, peaking at 1672 °C. The temperature at the specimen surface then declines sharply due to thermal conduction and surface emissivity.

Fig. 10 shows the top surface and cut-view, through thickness thermal damage profiles after multi-cell flux loading during a thermal

runaway event. The moderate damage area (areas where 300 °C ≤ T < 500 °C) was 27,035 mm^2 and extended eleven plies or 1.617 mm deep. The severe damage area (areas where T ≥ 500 °C) was 17,428 mm^2 and extended six plies deep or 0.882 mm.

Results for mechanical damage and residual strength will now be discussed.

3.3. Mechanical damage

In the thermo-mechanical models, the primary failure mechanism was delamination because of constrained thermal-expansion due to the combined effects of mechanical strain (from dynamic loading) and thermal strain (due to temperature transferred from the previous thermal damage simulation).

Fig. 11 shows the predicted delamination following both single- and multi-cell thermal runaway. The predicted delamination area and depth were 9930 mm^2 and six plies (0.88 mm), respectively, for the single cell case. The delamination area for the single cell case was 6% higher than the moderate thermal damage area predicted previously, and the delamination depth was two plies or 0.3 mm deeper than the predicted thermal damage.

The delamination area and depth for the multi-cell case were 33,779 mm^2 and twelve plies (1.76 mm), respectively. This delamination area was 25% larger than the moderate damage area. The delamination depth was 8.8% deeper than the thermal damage depth.

3.4. Residual strength prediction

In each CaTR simulation compressive failure propagated from the central thermo-mechanical damage region to the edges of the specimens. Fig. 12 shows the predicted strength-displacement plots for the undamaged, single- and multi-cell models. The strength of the undamaged specimen was 333 MPa. The presence of damage from a single cell runaway event reduced this by approximately 20% to 265 MPa while the damage from multi-cell runaway reduced the strength of the specimen by 56% to 146 MPa.

3.5. Summary and future work

The models herein have predicted damage following single- and multi-cell TR events on composite battery containment panels considering cylindrical 18650 battery cells. Table 6 provides a full summary of the simulation results. Results have shown that multi-cell loading doubled the predicted moderate thermal damage and trebled the severe thermal damage from the single cell case on a composite specimen. The peak temperature in the aluminium specimen increased by over six times from single cell to multi-cell loading. While temperature dependent properties were used for both aluminium and composite, the change in state of composite has a greater effect on damage. For example, around 500 °C or more, the matrix within the composite will change state and become

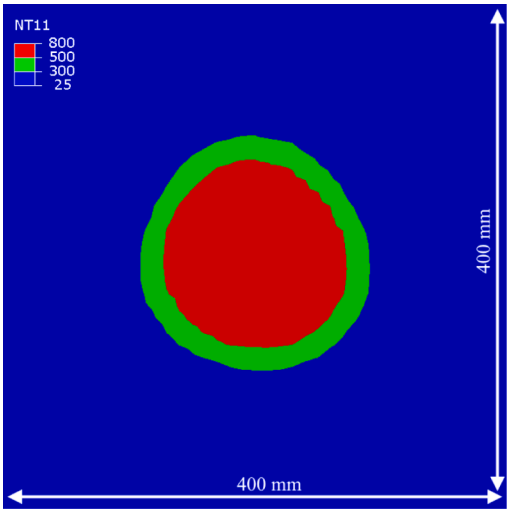

a) Top surface damage profile

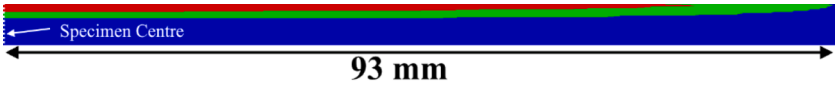

b) Through thickness damage profile

Fig. 10. Top surface and through thickness thermal damage after multi-cell flux loading (units are °C).

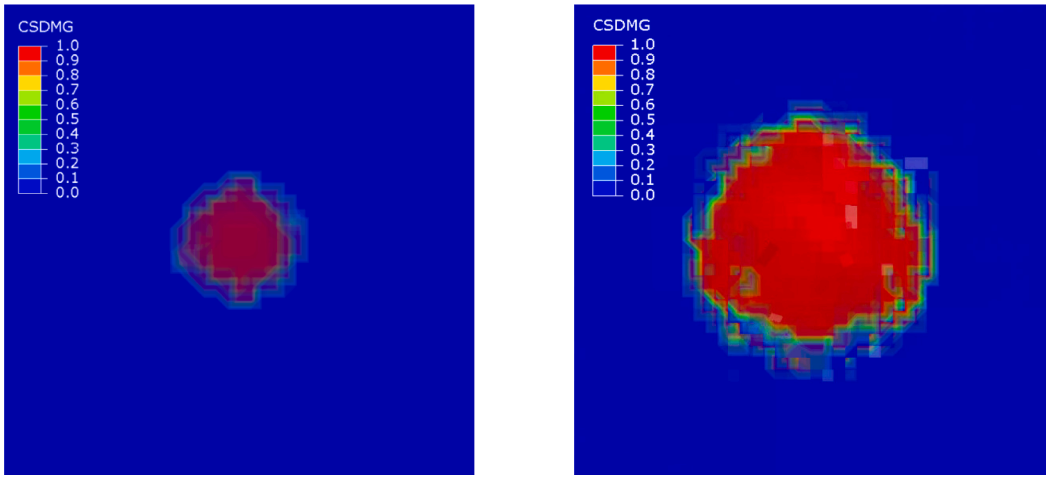

a) Delamination area after single cell loading *b) Delamination area after multi cell loading*

Fig. 11. Top view of predicted delamination following a) single cell and b) multi-cell thermal runaway.

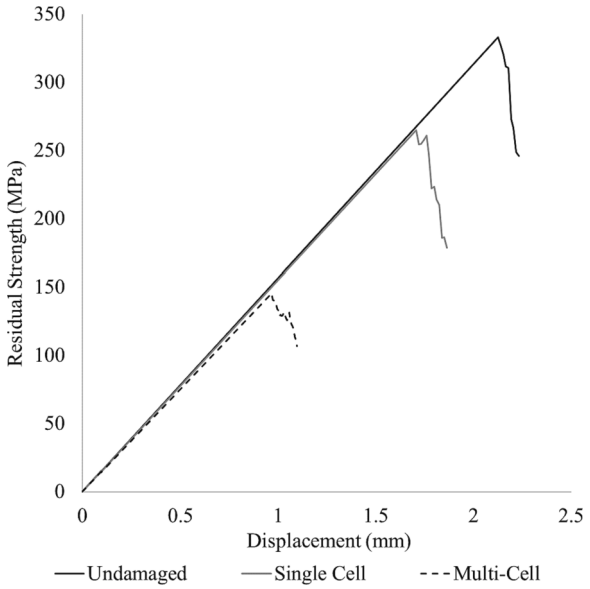

Fig. 12. CaTR plots for undamaged, single cell and multi-cell specimens.

Table 6
Results summary.

		Aluminium Single Cell	Multi-Cell	Composite Single Cell	Multi-Cell
Heat transfer model(s)	Peak temperature (°C)	127	831	656	1672
	Moderate thermal damage area (mm^2)	–	–	10,587	27,035
	Severe thermal damage area (mm^2)	–	–	5413	17,428
	Damage depth (plies/mm)	–	–	4 / 0.59	11 / 1.62
Thermo-mechanical model(s)	Delamination area (mm^2)	–	–	9930	33,779
	Delamination depth (mm)	–	–	6 / 0.88	12 / 1.76
Compression after Thermal Runaway (CaTR)	Residual strength (MPa)	–	–	265	146

char like. This creates a significant change in the material behaviour.

The models herein have not included pressure loading as this data has not been routinely characterised in experiments and the peak pressure is typically capped, using pressure relief valves, depending on the system. However, it is possible to estimate the effect of pressure loading from other extreme events. For example, research on lightning strikes has shown that the peak pressure could be 6.7 MPa [41] and if pressure loading was applied in isolation the effects were small. Rather, thermal loading associated with thermal strain/expansion had the largest contribution to thermo-mechanical damage. This observation is likely to be repeated for thermal runaway since the heating rates observed in single cell (~14,000 °C/min) and multi-cell runaway events (~16,000–24,300 °C/min) are comparable with those in lightning strike events (10,000–20,000 °C/min) [30]. Future work will include pressure loading, and ejected material in these models.

This future work could be aided by promising CFD models which are able to accurately predict experimental thermal runaway propagation and could be used as a guide for the TR initiation in subsequent cells following the initial onset of TR.

On-going work is currently using the modelling framework herein to compare and contrast different conductive protection materials for the improvement of lightweight composite battery containment structures, thus validating the ability of the model to be used as design tool for battery fire protection of composite enclosures. The framework herein would also allow the stochastic nature of battery thermal runaway to be studied. However, a large number of experimental and simulation tests would be required to generate statistical data.

4. Conclusions

The models presented herein have, for the first time, applied a simulation workflow to predict thermal and mechanical damage from a cylindrical 18650 lithium-ion batteries (LIB) thermal runaway (TR) event on a composite containment structure. A time dependent thermal loading profile was created and validated against experimental data for an aluminium plate specimen before this loading approach was applied to a composite material system. The cause and mechanisms of failure are captured and analysed using established modelling techniques and robust finite element codes supported by mature user subroutines to capture material behaviour.

The results have shown that for a 400 mm x 400 mm x 4.704 mm composite test specimen a single cell runaway event produced damage across 3% of the surface and penetrated 0.9 mm into the specimen (19% of the total depth). The damage from a multi-cell runaway event produced damage across 11% of the surface and penetrated 1.76 mm into the specimen (37% of the total depth). The presence of damage from a single cell runaway event can potentially reduce the strength of the specimen by 20% while multi-cell runaway can reduce the strength by 56%.

Future work will seek to further validate the models herein through experimentation as well as developing the methodology for prismatic and pouch cells. Other key physics such as pressure loading, and ejected material will also be added to better predict the potential damage and resulting reduction in residual strength.

While not directly proposing corrective actions, this paper proposes a modelling framework which could be used to compare and contrast different conductive protection materials for the improvement of lightweight composite battery containment structures, thus demonstrating the ability of the model to be used as design tool for battery fire protection of composite enclosures. Such predictive simulation capability should reduce the need for corrective action, minimising the number of physical tests to support design and certification, as well as aiding in the interpretation of physical test results.

CRediT authorship contribution statement

J. Sterling: Writing – original draft, Visualization, Validation, Software, Methodology, Investigation, Formal analysis. **L. Tattersall:** Writing – review & editing. **N. Bamber:** Writing – review & editing. **F. De Cola:** Writing – review & editing, Supervision. **A. Murphy:** Writing – review & editing, Supervision. **S.L.J. Millen:** Methodology, Software, Validation, Formal analysis, Investigation, Methodology, Writing – original draft, Supervision.

Declaration of competing interest

The authors declare that they have no known competing financial interests or personal relationships that could have appeared to influence the work reported in this paper.

Data availability

The authors do not have permission to share data.

Acknowledgements

This research did not receive any specific grant from funding agencies in the public, commercial, or not-for-profit sectors.

Appendix A. Supplementary data

Supplementary data to this article can be found online at https://doi.org/10.1016/j.engfailanal.2024.108163.

References

[1] X. Zeng, M. Li, D. Abd El-Hady, W. Alshitari, A.S. Al-Bogami, J. Lu, et al., Commercialization of lithium battery Technologies for Electric Vehicles, Adv Energy Mater. 9 (2019) 1900161, https://doi.org/10.1002/aenm.201900161.

[2] A. Wazeer, A. Das, C. Abeykoon, A. Sinha, A. Karmakar, Composites for electric vehicles and automotive sector: a review, Green Energy and Intelligent Transportation. (2022), https://doi.org/10.1016/j.geits.2022.100043.

[3] Z. Li, P. Zhang, R. Shang, Effects of heating position on the thermal runaway propagation of a lithium-ion battery module in a battery enclosure, Appl Therm Eng. 222 (2023) 119830, https://doi.org/10.1016/j.applthermaleng.2022.119830.

[4] J. Zhao, S. Lu, Y. Fu, W. Ma, Y. Cheng, H. Zhang, Experimental study on thermal runaway behaviors of 18650 li-ion battery under enclosed and ventilated conditions, Fire Saf J. 125 (2021) 103417, https://doi.org/10.1016/j.firesaf.2021.103417.

[5] B. Arief Budiman, S. Rahardian, A. Saputro, A. Hidayat, I. Pulung Nurprasetio, P. Sambegoro, Structural integrity of lithium-ion pouch battery subjected to three-point bending, Eng Fail Anal. 138 (2022) 106307, https://doi.org/10.1016/j.engfailanal.2022.106307.

[6] J. Xu, B. Liu, L. Wang, S. Shang, Dynamic mechanical integrity of cylindrical lithium-ion battery cell upon crushing, Eng Fail Anal. 53 (2015) 97–110, https://doi.org/10.1016/j.engfailanal.2015.03.025.

[7] J. Liu, Z. Wang, J. Bai, T. Gao, N. Mao, Heat generation and thermal runaway mechanisms induced by overcharging of aged lithium-ion battery, Appl Therm Eng. 212 (2022) 118565, https://doi.org/10.1016/j.applthermaleng.2022.118565.

[8] Y. Sun, Y. Jin, Z. Jiang, L. Li, A review of mitigation strategies for li-ion battery thermal runaway, Eng Fail Anal. 149 (2023) 107259, https://doi.org/10.1016/j.engfailanal.2023.107259.

[9] Y. Fu, S. Lu, K. Li, C. Liu, X. Cheng, H. Zhang, An experimental study on burning behaviors of 18650 lithium ion batteries using a cone calorimeter, J Power Sources. 273 (2015) 216–222, https://doi.org/10.1016/j.jpowsour.2014.09.039.

[10] Z. Liu, X. Guo, N. Meng, Z. Yu, H. Yang, Study of thermal runaway and the combustion behavior of lithium-ion batteries overcharged with high current rates, Thermochim Acta. 715 (2022) 179276, https://doi.org/10.1016/j.tca.2022.179276.

[11] A. Augeard, T. Singo, P. Desprez, M. Abbaoui, Contribution to the study of electric arcs in lithium-ion batteries, IEEE Trans Compon Packaging Manuf Technol. 6 (2016) 1066–1076, https://doi.org/10.1109/TCPMT.2016.2549502.

[12] Augeard A, Singo T, Desprez P, Perisse F, Menecier S, Abbaoui M. Arc analysis to the CID of li-ion battery cells in high-current applications. 2014 IEEE 60th Holm Conference on Electrical Contacts (Holm), 2014, p. 1–7. https://doi.org/10.1109/HOLM.2014.7031038.

[13] R. Mahamud, C. Park, Theory and practices of li-ion battery thermal Management for Electric and Hybrid Electric Vehicles, Energies (basel). (2022) 15, https://doi.org/10.3390/en15113930.

[14] Y. Zhang, W. Mei, P. Qin, Q. Duan, Q. Wang, Numerical modeling on thermal runaway triggered by local overheating for lithium iron phosphate battery, Appl Therm Eng. 192 (2021) 116928, https://doi.org/10.1016/j.applthermaleng.2021.116928.

[15] J. Lamb, C.J. Orendorff, L.A.M. Steele, S.W. Spangler, Failure propagation in multi-cell lithium ion batteries, J Power Sources. 283 (2015) 517–523, https://doi.org/10.1016/j.jpowsour.2014.10.081.

[16] J.G. Quintiere, On a method to mitigate thermal runaway and propagation in packages of lithium ion batteries, Fire Saf J. 130 (2022) 103573, https://doi.org/10.1016/j.firesaf.2022.103573.

[17] M. Mruzek, I. Gajdáč, Ľ. Kučera, D. Barta, Analysis of parameters influencing electric vehicle range, Procedia Eng. 134 (2016) 165–174, https://doi.org/10.1016/j.proeng.2016.01.056.

[18] Kerspe J, Fischer M. Requirements for battery enclosures – Design considerations and practical examples. In: Bargende M, Reuss H-C, Wagner A, Wiedemann J, editors. 19. Internationales Stuttgarter Symposium, Wiesbaden: Springer Fachmedien Wiesbaden; 2019, p. 1352–67.

[19] K. Pattarakunnan, J. Galos, R. Das, A.P. Mouritz, Impact damage tolerance of energy storage composite structures containing lithium-ion polymer batteries, Compos Struct. 267 (2021) 113845, https://doi.org/10.1016/j.compstruct.2021.113845.

[20] Y. Xia, T. Wierzbicki, E. Sahraei, X. Zhang, Damage of cells and battery packs due to ground impact, J Power Sources. 267 (2014) 78–97, https://doi.org/10.1016/j.jpowsour.2014.05.078.

[21] S. Xi, Q. Zhao, L. Chang, X. Huang, Z. Cai, The dynamic failure mechanism of a lithium-ion battery at different impact velocity, Eng Fail Anal. 116 (2020) 104747, https://doi.org/10.1016/j.engfailanal.2020.104747.

[22] X. Zhang, T. Zhang, N. Liu, X. Yin, X. Wu, H. Han, et al., Dynamic crushing behaviors and failure of cylindrical lithium-ion batteries subjected to impact loading, Eng Fail Anal. 154 (2023) 107653, https://doi.org/10.1016/j.engfailanal.2023.107653.

[23] X. Chen, Q. Yuan, T. Wang, H. Ji, Y. Ji, L. Li, et al., Experimental study on the dynamic behavior of prismatic lithium-ion battery upon repeated impact, Eng Fail Anal.. 115 (2020) 104667, https://doi.org/10.1016/j.engfailanal.2020.104667.

[24] P. Attar, J. Galos, A.S. Best, A.P. Mouritz, Compression properties of multifunctional composite structures with embedded lithium-ion polymer batteries, Compos Struct. 237 (2020) 111937, https://doi.org/10.1016/j.compstruct.2020.111937.

[25] A.P. Mouritz, S. Feih, E. Kandare, Z. Mathys, A.G. Gibson, P.E. Des Jardin, et al., Review of fire structural modelling of polymer composites, Compos Part A Appl Sci Manuf. 40 (2009) 1800–1814, https://doi.org/10.1016/j.compositesa.2009.09.001.

[26] C. Luo, J. Lua, P.E. Desjardin, Thermo-mechanical damage modeling of polymer matrix sandwich composites in fire, Compos Part A Appl Sci Manuf. 43 (2012) 814–821, https://doi.org/10.1016/j.compositesa.2011.03.006.

[27] T.W. Loh, E. Kandare, T.Q. Nguyen, The effect of thickness on the compression failure of composite laminates in fire, Compos Struct 286 (2022) 115334, https://doi.org/10.1016/j.compstruct.2022.115334.

[28] S. Feih, A.P. Mouritz, Tensile properties of carbon fibres and carbon fibre-polymer composites in fire, Compos Part A Appl Sci Manuf. 43 (2012) 765–772, https://doi.org/10.1016/j.compositesa.2011.06.016.

[29] S. Feih, Z. Mathys, A.G. Gibson, A.P. Mouritz, Modelling the tension and compression strengths of polymer laminates in fire, Compos Sci Technol. 67 (2007) 551–564, https://doi.org/10.1016/j.compscitech.2006.07.038.

[30] S.L.J. Millen, S. Ashworth, C. Farrell, A. Murphy, Experimental effects of heating rate on material properties for lightning strike simulations, Compos B Eng. (2022) 228, https://doi.org/10.1016/j.compositesb.2021.109438.

[31] K. Grigoriou, A.P. Mouritz, Influence of ply stacking pattern on the structural properties of quasi-isotropic carbon-epoxy laminates in fire, Compos Part A Appl Sci Manuf. 99 (2017) 113–120, https://doi.org/10.1016/j.compositesa.2017.04.008.

[32] J.-S. Kim, J.-C. Jeong, S.H. Cho, S.-I. Seo, Fire resistance evaluation of a train carbody made of composite material by large scale tests, Compos Struct. 83 (2008) 295–303, https://doi.org/10.1016/j.compstruct.2007.04.022.

[33] K. Grigoriou, A.P. Mouritz, Comparative assessment of the fire structural performance of carbon-epoxy composite and aluminium alloy used in aerospace structures, Mater Des. 108 (2016) 699–706, https://doi.org/10.1016/j.matdes.2016.07.018.

[34] P.T. Summers, B.Y. Lattimer, S. Case, S. Feih, Predicting compression failure of composite laminates in fire, Compos Part A Appl Sci Manuf. 43 (2012) 773–782, https://doi.org/10.1016/j.compositesa.2012.02.003.

[35] Y. Zhang, D. Kong, P. Ping, H. Zhao, X. Dai, X. Chen, Effect of a plate obstacle on fire behavior of 18650 lithium ion battery: an experimental study, J Energy Storage 54 (2022) 105283, https://doi.org/10.1016/j.est.2022.105283.

[36] Underwriters Laboratories Inc. UL2596, Battery Enclosure Thermal Runaway (BETR) Evaluation 2022.

[37] Zhu Z, Wang M, Zhang H, Zhang X, Yu T, Wu Z. A Finite Element Model to Simulate Defect Formation during Friction Stir Welding. Metals (Basel) 2017;7. https://doi.org/10.3390/met7070256.

[38] M. Sedighi, D. Afshari, F. Nazari, Investigation of the effect of sheet thickness on residual stresses in resistance spot welding of aluminum sheets, Proc Inst Mech Eng C J Mech Eng Sci. 232 (2018) 621–638, https://doi.org/10.1177/0954406216685124.

[39] J. Li, X. Li, G. Zhou, Y. Liu, Development and evaluation of a supersized aluminum flat plate heat pipe for natural cooling of high power telecommunication equipment, Appl Therm Eng. 184 (2021) 116278, https://doi.org/10.1016/j.applthermaleng.2020.116278.

[40] Shen J. Experimental Study on the Inhibition of Lithium Battery Combustion and Explosion in Different Atmospheric Nitrogen Environment. 2021.
[41] Millen SLJ, Murphy A. Understanding the influence of test specimen boundary conditions on material failure resulting from artificial lightning strike. Eng Fail Anal 2020;114. https://doi.org/10.1016/j.engfailanal.2020.104577.
[42] ABAQUS 2016 Documentation. ABAQUS Theory Manual. 2017.
[43] P. Foster, G. Abdelal, A. Murphy, Modelling of mechanical failure due to constrained thermal expansion at the lightning arc attachment point in carbon fibre epoxy composite material, Eng Fail Anal. 94 (2018) 364–378, https://doi.org/10.1016/j.engfailanal.2018.08.003.
[44] S.L.J. Millen, A. Murphy, G. Catalanotti, G. Abdelal, Coupled thermal-mechanical progressive damage model with strain and heating rate effects for lightning strike damage assessment, Appl. Compos. Mater. 26 (2019) 1437–1459, https://doi.org/10.1007/s10443-019-09789-z.
[45] M.L. Benzeggagh, M. Kenane, Measurement of Mixed-Mode Delamination Fracture Toughness of Unidirectional Glass/epoxy Composites with Mixed-Modebending Apparatus 56 (1996) 1–11.
[46] S.L.J. Millen, X. Xu, J. Lee, S. Mukhopadhyay, M.R. Wisnom, A. Murphy, Towards a virtual test framework to predict residual compressive strength after lightning strikes, Compos Part A Appl Sci Manuf. 174 (2023), https://doi.org/10.1016/j.compositesa.2023.107712.
[47] A. Kurzawski, L. Gray, L. Torres-Castro, J. Hewson, An investigation into the effects of state of charge and heating rate on propagating thermal runaway in li-ion batteries with experiments and simulations, Fire Saf J. 140 (2023) 103885, https://doi.org/10.1016/j.firesaf.2023.103885.
[48] J. Fang, J. Cai, X. He, Experimental study on the vertical thermal runaway propagation in cylindrical Lithium-ion batteries: effects of spacing and state of charge, Appl Therm Eng. 197 (2021) 117399, https://doi.org/10.1016/j.applthermaleng.2021.117399.